Electronic Supplementary Material (ESI) for Nanoscale.

Supplementary Information

Structural Dynamics and Activity of Nanocatalysts inside Fuel Cells by *in operando* Atomic Pair Distribution Studies

Valeri Petkov,[a,*] Shiyao Shan,[b] Binay Prasai,[a] Yang Ren,[c] Jinfang Wu[b], Hannah Cronk[b], Jin Luo[b], and Chuan-Jian Zhong [b,*]

[a)] Department of Physics, Central Michigan University, Mt. Pleasant, Michigan 48859, USA
[b)] Department of Chemistry, State University of New York at Binghamton, Binghamton, NY13902, USA
[c)] X-ray Science Division, Advanced Photon Source, Argonne National Laboratory, Argonne, Illinois 60439, USA

Methods:

i) Synthesis of binary Pd-Ni and ternary Pt-Ni-Co nanoparticle catalysts

For the synthesis of Pd-Ni nanoparticle (NP) catalyst, palladium(II) acetylacetonate and nickel(II) acetylacetonate were mixed in a desired molar ratio into a benzyl ether solvent. Oleic acid and oleylamine were added into the solution and used as capping agents. 1, 2-hexadecanediol was also added and used as a reducing agent. The solution was purged with N_2 and heated to 100 °C. At this temperature the purging with N_2 was discontinued, the mixture heated to 220 °C and refluxed for 30 min. After the solution cooled back to room temperature, the resulting Pd-Ni NPs were precipitated out by adding ethanol followed by centrifugation. The NPs were then dried under N_2 atmosphere and re-dispersed in hexane for future use.

For the synthesis of Pt-Ni-Co NP catalyst, $Pt^{II}(acac)_2$, $Ni^{II}(acac)_2$, and $Co^{III}(acac)_3$ were mixed in a desired molar ratio into an octyl ether solvent. Oleylamine and oleic acid were added into the solution and used as capping agents. 1,2-hexadecanediol was also added and used as a reducing agent. The solution was purged with N_2 and heated to 105°C. At this temperature the purging with N_2 was discontinued, the mixture heated to 280 °C and refluxed for 40 min. After the solution cooled back to room temperature, the resulting Pt-Ni-Co NPs were precipitated out by adding ethanol followed by centrifugation. The NPs were then dried under N_2 atmosphere and re-dispersed in hexane for future use.

So-synthesized Pd-Ni and Pt-Ni-Co NPs were activated for catalytic applications, in particular for oxygen reduction reaction (ORR), by a commonly applied procedure including depositing the NPs on fine carbon (XC-72) powder followed by a thermal treatment. In particular, controlled amounts of Pd-Ni and Pt-Ni-Co NPs were mixed with carbon powder in a hexane solution followed by sonication and overnight stirring. The resulting carbon supported NPs were collected and dried under N_2 atmosphere. The dry NPs were treated at 260 °C under 20 vol % O_2 atmosphere for 1 h to remove the organic molecules capping their surface. The NPs were then calcined at 400 °C under 15 vol % H_2 atmosphere for 2h. Hereafter, for the sake of simplicity, the activated for ORR, carbon supported Pd-Ni and Pt-Ni-Co NPs are referred to as as-synthesized NPs.

ii) *Determining the overall chemical composition, size, shape and chemical pattern of Pd-Ni and Pt-Ni-Co NPs*

The overall chemical composition of Pd-Ni and Pt-Co-Ni NPs, as-synthesized and then tested as ORR catalysts, was determined by inductively coupled plasma atomic emission spectroscopy (ICP-AES). Measurements were done on a Perkin Elmer 2000 DV ICP-OES instrument. Batches of the respective NPs were dissolved in aqua regia and then diluted to concentrations in the range of 1 to 50 ppm. Calibration curves were made from dissolved standards in the same acid matrix as the unknowns. Standards and the unknowns were analysed several times each resulting in < 3 % error in the overall chemical composition.

Experimental ICP-AES data showed that the chemical composition of as-synthesized Pd-Ni and Pt-Ni-Co NPs NPs is $Pd_{30}Ni_{70}$ and $Pt_{45}Ni_{33}Co_{22}$, respectively. The composition of Pd-Ni NPs studied *ex situ*, i.e. inside a standard electrochemical cell cycled 400, 1000 and 3000 times between 0.4 V and 1.0 V turned out to be $Pd_{39}Ni_{61}$, $Pd_{46}Ni_{54}$ and $Pd_{69}Ni_{31}$, respectively. The chemical composition of Pd-Ni NPs studied *in operando*, i.e. as deposited on the cathode of an operating proton exchange membrane fuel cell (PEMFC) cycled 3000 times between 0.6 V and 1.2 V was found to be $Pd_{82}Ni_{18.}$ The chemical composition of Pt-Co-Ni NPs studied *ex situ*, i.e. inside a standard electrochemical cell cycled 400, 1000 and 3000 times between 0.6 V and 1.0 V turned out to be $Pt_{56}Ni_{25}Co_{19}$, $Pt_{57}Ni_{24}Co_{19}$ and $Pt_{59}Ni_{23}Co_{18}$, respectively. The chemical composition of Pt-Ni-Co NPs studied *in operando*, i.e. as deposited on the cathode of an operating PEMFC cycled 3000 times between 0.6 V and 1.2 V was found to be $Pt_{60}Ni_{22}Co_{18}$. Results indicated that Pd-Ni and Pt-Ni-Co NPs lose a substantial amount of transition metal (TM) species during both the *ex situ* and *in operando* studies via a process known as "leaching of TM species". The relative amount of TM species (in %) retained in Pd-Ni and Pt-Ni-Co NPs undergone a particular number of electrochemical cycles inside a 3-electrode cell is presented in Figure 3.

The diameter, hereafter referred to as size, and shape of as-synthesized and electrochemically cycled Pd-Ni and Pt-Ni-Co NPs were determined by Transmission Electron Microscopy (TEM) on a JEM-2200FS instrument operated at 200 kV. Exemplary TEM and high-resolution (HR)-TEM images are summarized in Figures 1, 4, and 5. Images in Figure 1 show that as-synthesized Pd-Ni and Pt-Ni-Co NPs are approximately 7.1 (±0.6) nm 7.3 (±0.6) nm in size, respectively. As can be seen in Figure 4, the size of Pd-Ni NPs studied inside a standard electrochemical cell cycled 400, 1000 and 3000 times between 0.6 and 1.0 V increases to 7.5 (±0.6) nm, 8.2 (±0.7) nm and 8.9 (±0.8) nm, respectively. Images in Figures 1 and 5 show that as-synthesized Pt-Ni-Co NPs are approximately 7.3 (±0.6) nm in size. The size of Pt-Ni-Co NPs studied inside a standard electrochemical cell cycled 400, 1000 and 3000 times between 0.6 V and 1.0 V is 7.7 (±0.6) nm, 8.4 (±0.7) nm and 9.1 (±0.8) nm, respectively. Evidently, NM-TM nanocatalysts concurrently lose TM species and increase in size during ORR activity tests conducted on a standard 3-electrode cell. .

The size of Pd-Ni and Pt-Ni-Co NPs, as-synthesized and then tested as ORR catalysts, was also determined by analysis of the width of Bragg-like peaks in their *ex situ* and *in operando* high-energy x-ray diffraction (HE-XRD) patterns using the Scherrer formalism [S1]. In particular, per *ex situ* HE-XRD data shown in Figure S5, as-synthesized Pd-Ni NPs are approximately 6.9 (±0.7) nm in size. The size of NPs increases to 7.4 (±0.7) nm, 8.1 (±0.7) nm and 8.8 (±0.7) nm when they undergo, respectively, 400, 1000 and 3000 electrochemical cycles inside a standard 3-electrode cell. Per *ex situ* XRD data, as-synthesized Pt-Ni-Co NPs are approximately 7.4 (±0.7) nm in size. The size of NPs increases to 7.5 (±0.7) nm, 8.3 (±0.7) nm and 8.9 (±0.7) nm when they undergo, respectively, 400, 1000 and 3000 electrochemical cycles inside a standard 3-elctrode cell. Results show that HE-XRD determined NP sizes come pretty close to TEM determined NP sizes. Hence, the rate of increase in the size of NM-TM NPs inside operating fuels cells can be determined precisely by HE-XRD.

The size of *in operando* studied Pd-Ni and Pt-Ni-Co NPs was determined by analysis of the width of Bragg-like peaks in their HE-XRD patterns shown in Figures S6 and S7, respectively. Per the *in operando* HE-XRD data, Pd-Ni and Pt-Ni-Co NPs NPs gradually increase in size, respectively, from 6.9 (±0.7) nm to about 9.1 (±0.7) nm and from 7.4 (±0.7) nm to about 9.0 (±0.7) during 3000 PEMFC cycles. Changes in the size of TM-MN NPs during the *ex situ* and *in operando* studies, are summarized in Figures 3 and 12, respectively, in terms of changes in the so-called Geometric Surface Area (GSA). The latter is nothing but the reciprocal of NP size. As TEM and HR-TEM images in Figures 1, 4 and 5 show, Pd-Ni and Pt-Ni-Co NPs, as-synthesized and then tested as ORR catalysts, are largely spherical in shape.

The chemical pattern of Pd-Ni and Pt-Ni-Co NPs, as synthesized and tested as ORR catalysts inside a standard electrochemical cell, was determined by High-Angle Annular Dark-Field (HAADF) Scanning TEM (STEM). The experiments were done on a FEI Titan G2 80-200S STEM microscope operated at 200 kV. Exemplary HAADF-STEM images and elemental maps of as-synthesized Pd-Ni and Pt-Co-Ni NPs and of Pd-Ni and Pt-Ni-Co NPs undergone 3000 cell cycles are shown in Figures 2 and 6, respectively. HAADF-STEM images and the respective elemental maps indicate that both as-synthesized and electrochemically cycled Pd-Ni and Pt-Ni-Co NPs are largely random-type alloys.

iii) *X-ray photoelectron spectroscopy (XPS)* measurements

XPS was used to determine the oxidation state and abundance of NM (Pd and Pt) and TM (Ni and Co) species at the surface of as-synthesized Pd-Ni and Pt-Ni-Co NPs. Measurements were carried out on a Physical Electronics Quantum 2000 scanning ESCA microprobe. The system uses a focused monochromatic Al Kα X-ray (1486.7 eV) source for excitation, a spherical analyzer and a 16-element multichannel detector. The binding energy (BE) scale of the instrument was calibrated using C 1s peak at 284.8 eV, Cu $2p_{3/2}$ peak at 932.62 eV and Au $4f_{7/2}$ peak at 83.96 eV as internal standards. The percentages of individual atomic species at the NP surface were determined by analyzing the areas of respective XPS peaks. As an example, XPS spectra for as-synthesized Pt-Ni-Co NPs are shown in Figure S1. The XPS determined surface composition of as-synthesized Pt-Ni-Co NPs was found to be $Pt_{46}Ni_{34}Co_{20}$ and that of as-synthesized binary Pd-Ni NPs - $Pd_{24}Ni_{76}$. So-determined NP surface composition appeared very close to the ICP-AES determined bulk composition of $Pt_{45}Ni_{33}Co_{22}$ and $Pd_{30}Ni_{70}$, respectively. The result indicated that, in line with HAADF-STEM imaging, as-synthesized Pd-Ni and Pt-Ni-Co NPs are near random alloys. The BE values for Pd $3d_{5/2}$ and Ni $2p_{3/2}$ in as-synthesized Pd-Ni NPs were observed at 335.9 eV and 856.6 eV. For comparison, the values of BE for metallic Pd(0) and Ni(0) are 335.0 eV and 852.6 eV, respectively, and that for oxidized Ni(+2) is 855.6 eV. The BE values for Pt $4f_{7/2}$, Ni $2p_{3/2}$ and Co $2p_{3/2}$ in as-synthesized Pt-Ni-Co NPs were observed at 71.7 eV, 856.6 eV and 780.7 eV, respectively. For comparison, the values of BE for metallic Pt(0) and Co(0) are 71.0 eV and 778.2 eV, respectively, and that for oxidized Co(+2) is 779.7 eV. Apparently, NM species (Pd and Pt) at the surface of as-synthesized Pd-Ni and Pt-Ni-Co NPs were largely in metallic state while TM ones (Ni and Co) were somewhat oxidized. The observed partial oxidation of surface TM species in as-synthesized NM-TM NPs studied here may be explained with the fact that the NP samples were exposed to air prior the XPS measurements.

iv) Ex situ studies on the ORR activity of Pd-Ni and Pt-Ni-Co

The ORR activity of Pd-Ni and Pt-Ni-Co NPs was tested by cyclic voltammetry (CV) and rotating disk electrode (RDE) experiments carried out on a standard (laboratory) 3-electrode electrochemical cell coupled to a microcomputer-controlled analyzer (CHI 600a, CH Instruments). Data was taken at room temperature. The NP samples were loaded on the working electrode of the cell following usual procedures. The electrolyte in the cells (0.1 M $HClO_4$) was de-aerated with high purity N_2 before the CV experiments and saturated with O_2 before the RDE ones. CV and RDE data was collected for as-synthesized NPs and for NPs undergone 400, 1000 and 3000 electrochemical cycles between 0.4 and 1.0 V at a rate of 100 mV/s. The applied voltage had a triangular profile. As an example, CV and RDE data sets for as-synthesized and electrochemically cycled Pt-Ni-Co NPs are shown in Figure S2.

Experimental CV and RDE data sets were analyzed and the electrochemical active surface area (ECSA), mass (MA) and specific activity (SA) of Pd-Ni and Pt-Ni-Co NPs for ORR were obtained as a function of the number of electrochemical cycles. In particular, ECSAs values (summarized in Table S1) were obtained by integrating the charge in the H_{UPD} range (hydrogen absorption region) in the respective CV data sets. MAs values (summarized in Table S1) were obtained from the kinetic currents, i_k, of the respective RDE data sets. Note, i_k was measured at voltages ~ 0.9 V, i.e. close to the actual Open Circuit Voltage (OCV) of PEMFCs. As studies have shown mass-transport and Ohmic losses (see *eq.* 1 in the text) in the current output of PEMFCs/3-electrode cells would be reduced to a minimum at operating voltages close to the OCV [S2]. Inspection of data in Table S1 shows that the ORR (MA) activity both of Pd-Ni and Pt-Ni-Co NPs decreases with the number of electrochemical cycles. The rate of decay of the (MA) ORR activity of Pd-Ni and Pt-Ni-Co NPs with the number of electrochemical (cell) cycles is presented in Figure 3.

For the purposes of our study, the electrocatalytic measurements were discontinued after the cell was cycled 400, 1000 and 3000 times and NPs scraped off its working electrode under protective atmosphere. The chemical composition, chemical pattern, size and shape of these NPs were determined by ICP-AES, HAADF-STEM (see Figures 2 and 6) and TEM (see Figures 4 and 5). The NPs (sealed between Kapton sheets) were also studied by high-energy synchrotron x-ray diffraction (HE-XRD). Exemplary HE-XRD patterns are shown in Figure S5. Note, results from all experiments described above are referred to as *"ex situ"* since they pertain to Pd-Ni and Pt-Ni-Co NPs studied outside an operating PEMFC.

v) In operando studies on the ORR activity of Pd-Ni and Pt-Ni-Co NPs

A fully functional PEMFC optimized for HE-XRD experiments was constructed to assess the concurrent changes in the atomic structure and ORR activity of Pd-Ni and Pt-Ni-Co NPs under realistic operating conditions. Schematic of the PEMFC is shown in Figure S3. To minimize unwanted x-ray scattering from the PEMFC hardware, a 5 mm hole was drilled through the PEMFC anode side down to the sheet of carbon paper (Spectracarb 2050A-0550) used as hydrogen diffusion layer. A spherical window was cut through the PEMFC cathode side this time down to the sheet of carbon paper used as oxygen diffusion layer. Thin Kapton foil, that is virtually transparent to high-energy x-rays, was used to seal the outer sides of the PEMFC.

Membrane electrode assemblies (MEAs), with an active area of 6.25 cm^2, were prepared using either as-synthesized Pd-Ni ($Pd_{30}Ni_{70}$) (40 % metal loading, 0.6 mg_{Pd} cm^{-2}) or Pt-Ni-Co ($Pt_{45}Ni_{33}Co_{22}$) NPs (50 % metal loading, 0.8 mg_{Pt} cm^{-2}) as an ORR catalyst at the PEMFC cathode. Commercial Pt NPs (20 % Pt/C, E-tek, 0.08 mg_{Pt} cm^{-2}) were used as a HOR (hydrogen oxidation reaction) catalyst at the PEMFC anode. In particular, the respective (carbon-supported) metallic NPs were dissolved in 5 wt% Nafion-containing solution as to achieve NP concentration of 2-3 mg/mL. The so-prepared catalyst-Nafion ink was brush coated on the wet-proof carbon paper. The anode and cathode catalyst coated carbon paper was fused to the respective sides of a Nafion membrane (Nafion 212 membrane, DuPont) by hot pressing at 120 ^{o}C. The resulted sandwich-type {Carbon Paper-Anode Catalyst-Nafion Membrane-Cathode Catalyst-Carbon Paper} assembly (see Figure S3) was transferred to the custom-made PEMFC under protective atmosphere. During the measurements high purity hydrogen gas (3.5% H_2 balanced by He) was fed to the PEMFC anode compartment at a rate of 50 mL/min. Before reaching the anode, the gas was forced through a water bubbler to achieve 100 % humidity. High-purity nitrogen gas was flown through the PEMFC cathode compartment. Catalysts at the cathode side of respective MEAs were subjected to an accelerated test for ORR activity and stability by cycling the PEMFC between 0.6 to 1.2 V at a scan rate of 100 mV/s. The applied voltage had a triangular profile. The PEMFC anode was used as a voltage reference electrode and the PEMFC cathode side was used as a working electrode. The current output of the PEMFC was non-stop recorded during the voltage cycling which lasted for about 12 h so that a preset number of 3000 PEMFC cycles is reached. Exemplary polarization curves showing the current output of the PEMFC resulted from the repetitive application of external voltages are shown in Figure S4. The curves are typical for ORR catalysts subjected to accelerated stability tests of the type recommended by DOE [S11] [e.g. see Figure 2 in refs. [S3]). As data in Figure S4 show, the current output of the PEMFC decreases with the number of voltage cycles.

As discussed in the text, and as shown in studies of others [S3, S4], the SA (related to activation losses) and ECSA (related to exchange current density/relative number of active sites at the surface of the nanocatalyst used at the PEMFC cathode) of nanocatalysts exhibiting high ORR activity would be high resulting in an ample current output of the PEMFC (see *eqs.* 1 and 2 in the text). On the other hand, when the SA and/or ECSA of nanocatalysts for ORR diminish, the current output of the PEMFC would diminish too. According to the results of our *in operando* studies, the rate of decrease in the PEMFC current output with the number of voltage cycles is much smaller when Pt-Ni-Co NPs are used as the PEMFC cathode catalyst as compared to the case when Pd-Ni NPs are used instead (see data in Figure S4). That is to be expected since, per our *ex situ* electrocatalytic studies, Pt-Ni-Co NPs are more stable as an ORR catalyst in comparison to Pd-Ni ones (see data in Figure 3 and Table S1). The observations indicates that the *in operando* observed rate of decrease in the current output of the PEMFC can be used as a measure of the rate of decrease in the ORR (MA) activity of the PEMFC cathode catalysts. The rate of decrease in the ORR (MA) activity of Pd-Ni and Pt-Ni-Co NPs, as derived from the rate of decrease in the current output of the PEMFC measured at 0.9 V on the respective polarization curves, is shown in Figure 12. Here it may be noted that considering the rate of change in the PEMFC current output as a measure of the rate of change in the ORR (MA) activity of Pd-Ni and Pt-Ni-Co NPs is based on the assumption that the amount of nanocatalyst loaded on the PEMFC cathode does not change during the PEMFC cycling. Tests for ORR activity and stability conducted on standard 3-electrode electrochemical cells largely rely on the same assumption. Also, considering the rate of change in the PEMFC current output as a measure of the rate of change in the ORR (MA) activity of Pd-Ni and Pt-Ni-Co NPs assumes that, as being cycled, the PEMFC does not suffer major hardware failures such as, for example, puncturing of the MEA. Such failures would result in erratic changes in the current output of the PEMFC. We did not observe any erratic changes in the current output of the PEMFC during the *in operando* studies, as data in Figure S4 testify.

vi) *Ex situ and in operando atomic pair distribution studies on Pd-Ni and Pt-Ni-Co NPs*

High-energy synchrotron x-ray diffraction (HE-XRD) experiments were carried out at the 11-ID-C beamline of the Advanced Photon Source at the Argonne National Laboratory using x-rays with energy of 115 keV (λ=0.1080 Å). A large area detector allowing fast data collection rates was used to collect the HE-XRD patterns. Diffracted x-ray intensities were measured to wave vectors of 25 Å^{-1} allowing resolving the structural features of Pd-Ni and Pt-Ni-Co NPs in good detail. The experimental set-up was calibrated with high-purity Si powder standard.

XRD patterns for Pd-Ni and Pt-Ni-Co NPs tested as ORR catalysts on the standard electrochemical cell were obtained using samples scraped off the cell's working electrode, as described above, and sealed between Kapton foils. Kapton foil alone was measured separately. Experimental *ex-situ* XRD patterns of Pd-Ni and Pt-Ni-Co NPs, as corrected for sample absorption, Kapton foil and other background-type (air etc.) scattering, are shown in Figure S5.

In operando HE-XRD patterns for Pd-Ni and Pt-Ni-Co NPs (sandwiched in MEAs assemblies and positioned inside the operating PEMFC) were collected while the PEMFC was cycled between 0.6 and 1.2 V. The patterns were measured in intervals of 3 min, for 1 min each, over a period of 12 h necessary to reach a preset number of 3000 PEMFC cycles. HE-XRD patterns for the PEMFC without a MEA assembly in it and for the PEMFC with a MEA assembly in it that does not contain the cathode (ORR) catalyst were measured separately. The patterns were used to correct the HE-XRD data taken while the PEMFC was cycled. Experimental *in operando* HE-XRD patterns for Pd-Ni and Pt-Ni-Co NPs, as corrected for the PEMFC hardware and other background-type (air etc.) scattering, are shown in Figures S6 and S7, respectively. As data in Figures S5, S6 and, S7 show, both the *ex situ* and *in operando* obtained XRD patterns for Pd-Ni and Pt-Ni-Co nanocatalysts exhibit a few Bragg-like features at low diffraction angles and almost no sharp features at high diffraction angles, i.e. are rather diffuse in nature. This rendered the well-established, sharp Bragg peaks-based procedures for determining the atomic-scale structure of bulk metals and alloys inapplicable to the NPs studied here. Therefore, following well-established procedures [S4], the diffuse *in operando* HE-XRD patterns of Figures S5, S6 and S7 were reduced to the so-called atomic PDFs G(r). *Ex situ* obtained G(r)'s for Pd-Ni and Pt-Ni-Co NPs are shown in Figure 7. *In operando* obtained G(r)'s for Pd-Ni and Pt-Ni-Co NPs are shown in Figures S8 and S9, respectively. Colour maps of the *in operando* PDFs are shown in Figure 16 (lower panel). The PDF approach is advantageous since, contrary to the respective diffuse HE-XRD patterns, atomic PDFs show several distinct peaks allowing convenient testing and refinement of 3D structure models for metallic NPs [S5-S7]. Here it is to be underlined that experimental HE-XRD patterns, and so the atomic PDFs derived from them, reflect ensemble averaged structural features of all metallic NPs sampled by the x-ray beam in a way traditional powder XRD patterns reflect ensemble averaged structural features of all polycrystallites sampled by the x-ray beam in those experiments. Using NP ensemble averaged structural features to understand and explain NP ensemble averaged properties (e.g. catalytic, magnetic, optical etc.) puts the exploration of the atomic structure and the properties of metallic NPs on the same footing. Note, by definition, atomic PDFs G(r) peak at distances separating all pairs of atoms within the nanometer-sized material studied. Accordingly, the experimental PDFs shown in Figures 7, S8, S9 and 16 peak at distances separating pairs of TM-TM, TM-NM and NM-NM atoms (TM=Ni and Co; NM=Pd and Pt), immediate and all farther neighbours, within the respective NPs. Furthermore, the area under the PDF peaks is proportional to the number of atomic pairs at those distances. Hence, the *ex situ* and *in operando* PDFs considered here indeed are sensitive both to the configuring, as reflected by atomic-pair distances, and relative amount of TM and NM atoms in Pd-Ni and Pt-Ni-Co NPs.

Another important point is to made here: Since surface atoms at the opposite sides of NPs are separated the most, experimental G(r)s would show distinct peaks *only* up to distances close to the average size of the particular NPs studied, as demonstrated in Figure S10(b). Clearly, peaks at those higher-r distances would largely reflect pairs of atoms close to the NP surface. Hence, experimental atomic PDFs for metallic NPs used in catalytic applications, in particular the PDF data at higher -r values, are sensitive to the arrangement of atoms at the NP surface whereat chemical reactions tale place. Accordingly, 3D models refined against experimental PDF data, such as the 3D models shown in Figures S10(a) and 10, can provide an accurate description of the atomic arrangement in metallic NPs, including that at the NP surface. This fact may not come as a surprise since atoms at the surface of metallic NPs used in catalysis (typically < 15 nm) occupy a substantial fraction of the NP volume and HE-XRD is known to be volume sensitive (down to a few %) technique [S1, S5]. For reference, atoms in the top two layers of as-synthesized, *ex situ* and *in operando* studied Pd-Ni and Pt-Ni-Co NPs, that determine the geometrical landscape and electronic structure of the NP surface, are about 25 to 30 % of all atoms in the NPs (see the 3D model shown in the lower right corner in Figure S10(b).)

vii) *Modeling the 3D atomic structure of Pd-Ni and Pt-Ni-Co NPs by Molecular Dynamics*

3D atomic models for as-synthesized, *ex situ* and *in operando* studied Pd-Ni and Pt-Co-Ni NPs, were built by classical Molecular Dynamics (MD) simulations based on the simple but proven highly efficient quantum corrected Sutton-Chen (SC) method [S14-S16]. In brief, the method considers atomic pair interactions in metals and alloys as a sum of two constituents. One accounts for the repulsion between metal atom cores and the other - for the attractive force between metal atom cores due to the electrons surrounding them. Accordingly, the energy of atomic-level models, *U,* appears as a sum of an atomic pair potential $V(r_{ij})$ term and a local electron density (ρ_i) term defined as follows:

$$U = \sum_{i} \left[\sum_{j \neq i} \frac{1}{2} h_i \epsilon_{ij} V(r_{ij}) - c_i \epsilon_{ij} (\rho_i)^{\frac{1}{2}} \right] \qquad \text{(S1)}$$

where

$$V(r_{ij}) = \left(\frac{a_{ij}}{r_{ij}} \right)^{n_{ij}} \quad \text{and} \quad \rho_i = \sum_{j \neq i} \left(\frac{a_{ij}}{r_{ij}} \right)^{m_{ij}} \qquad \text{(S2).}$$

The so-called "energy" parameter $\epsilon_{ij}(meV)$ and the dimensionless parameter c_i are used to scale appropriately the interatomic repulsive $V(r_{ij})$ and attractive (ρ_i) metal-to-metal interactions, respectively. Parameters m_{ii} and n_{ii} are positive integers such that $n_{ii} < m_{ii}$. Parameter a_{ij} is a quantity used to scale appropriately distances r_{ij} between i and j type atoms in structure models, including the shortest ones (that are nothing but metal-to-metal bonding distances). SC parameters for Pd, Ni, Pt and Co were taken from literature sources [S16, S17]. The interactions between unlike atoms, i.e. *i-j* type atomic interactions, were estimated by a mixing rule described in Ref. [S18].

Since, in general, the realism of classical MD simulations is dependent both on the structure models chosen and conditions under which the simulations are run, the initial model atomic configurations considered here reflected the size (~ 11000 to 15000 atoms), shape (spherical) and chemical composition of actual Pd-Ni and Pt-Ni-Co NPs modeled (as determined by TEM and ICP-AES experiments described above). The configurations featured several plausible phase states of Pd-Ni and Pt-Ni-Co NPs, including random alloy, distinct core-distinct shell, distinct core-inhomogeneous shell, Janus and sandwich-type phase states (see Figures S11 and S12). The configurations were optimized in terms of energy, i.e. stabilized at atomic level, with the help of the computer program DL-POLY [S19]. The optimization was performed under canonical NVT ensemble in the absence of periodic boundary conditions. Velocity Verlet algorithm with a time step of 2 fs was used.

Typically, MD simulations on metallic systems involve quenching of atomic configurations equilibrated at pretty high temperature (often above melting temperature). However, as it is the common practice in nanocatalysis, Pd-Ni and Pt-Ni-Co NPs studied here were synthesized in solution at room temperature and then subjected to a post-synthesis treatment at 400 ^{o}C, i.e. they were not obtained by quenching from a melt. Hence, the initial atomic configurations were not melted but equilibrated for 200 ps at 400 ^{o}C. That temperature reflects the post-synthesis treatment (calcination) of Pd-Ni and Pt-Ni-Co NPs. Otherwise, MD optimized models appeared highly disordered structurally and so completely inconsistent with the findings of TEM, HR-TEM and HE-XRD studies described above. After the initial equilibration at 400 ^{o}C, the configurations were cooled down to room temperature (300K) in steps of 50 K and again equilibrated for 100 ps.

On the other hand, typically, MD simulations featuring initial atomic configurations cut out from a single crystal structure and then equilibrated at temperature below melting, produce NP models that are well too ordered structurally, especially close to the model's surface. The reason is that MD treats all atoms in structure models alike whereas atoms inside and at the surface of actual metallic NPs are not necessarily alike in respect to their immediate atomic neighborhood, and others [S12, S20]. Hence, after being equilibrated at 400 ^{o}C and then cooled down to room temperature, each of the model configurations was equilibrated further at 500 K for 100 ps as to mimic (as much as possible) the usual atomic positional disorder in metallic NPs < 15 nm. Altogether, MD models for Pd-Ni and Pt-Ni-Co NPs built here are with realistic size, shape, chemical composition and energy, i.e. atomic level stability, optimized to the fullest possible extent. As such, though not perfect, the models provide a realistic basis for ascertaining the phase state of Pd-Ni and Pt-Ni-Co NPs through comparing the model computed atomic PDFs with experimental atomic PDFs, as demonstrated in Figures 8 and 15. Ascertaining the phase state of materials, known as "phase-analysis", by comparing experimental XRD patterns with patterns for reference phases (stored in databases) is a widely applied practice in materials science. Furthermore, the MD models found to approach the experimental atomic PDFs the best, as compared to the other MD models considered, served as an excellent starting point for the hybrid RMC simulations described below.

Note, Fourier transformation is a unitary operation and so structure-relevant information in experimental XRD data is not modified in any way when that data are represented in terms of atomic PDFs, a quantity defined in real space. Indeed, it is a matter of convenience and practicality to decide how to analyze experimental XRD data, as obtained in reciprocal (diffraction space) or as Fourier transformed in real space.

viii) Evaluating the quality of 3D structure models for Pd-Ni and Pt-Ni-Co NPs

The quality of MD simulated and hybrid RMC refined 3D models for Pd-Ni and Pt-Ni-Co NPs was evaluated by computing model's quality factors, R_w, defined as [S5, S6, S21]:

$$R_w = \left\{ \frac{\sum w_i (G_i^{\exp.} - G_i^{calc.})^2}{\sum w_i (G_i^{\exp.})^2} \right\}^{1/2} \tag{S3}$$

where $G^{exp.}$ and $G^{calc.}$ are the experimental and model computed atomic PDFs, respectively, and w_i are weighting factors reflecting the experimental uncertainty of individual $G^{exp.}$ data points. Here w_i were considered to be uniform which, as predicted by theory [S21] and largely corroborated by experiment [S22], is a reasonable approximation in the case of high quality G(r) data such as ours. Typical values of R_w for good-quality 3D models refined against experimental atomic PDFs are in the range of 15-30 % [S5, S6, S21]. However, MD models considered here are based on theory (SC method)) and do not take into account the experimental PDF data. Hence, values of R_w reported in Figures 8 and 15 appear somewhat higher than the typical ones. The inherently higher values of quality factors R_w for the MD models though did not affect the functional purpose of R_w as a quantity allowing discriminating between the models on an objective basis. Note, values of R_w reflect the overall quality of 3D structure models. Difference between 3D model-derived and experimental PDFs data shows how well individual features in the latter are reproduced by the former thus providing another stringent criteria for evaluating the quality of 3D models for NPs [S23, S24]. Both values of R_w*'s* and difference curves are used here for evaluating the quality structure models for Pd-Ni and Pt-Ni-Co NPs unambiguously (see Figures 8, 9 and 15).

ix) Hybrid reverse Monte Carlo Simulations

Hybrid Reverse Monte Carlo (RMC) simulations were used to refine further the MD models that, when compared to all other MD models considered, were found to reproduce best the experimental atomic PDFs for as-synthesized, *ex situ* and *in operando* studied Pd-Ni and Pd-Ni-Co NPs. As discussed above, the refinement of MD optimized models against experimental PDF data is very much necessary since MD simulations alone cannot capture well details of the surface structure of metallic NPs. The details are important since it is the NP surface whereat chemical reactions take place. In the spirit of traditional RMC simulations [S25, S26] the positions of atoms in the MD optimized models were adjusted as to minimize the difference between the model-computed and respective experimental atomic PDFs. Note, the MD models used as a "starting point" of hybrid RMC simulations are with realistic size, shape and chemical composition. Furthermore, the models are optimized in terms of energy, i.e. stabilized at atomic level, and feature phase state consistent with the experimental PDF data and, where applicable, with HAADF-STEM images. During the simulations atoms in the MD models were constrained to maintain as maximal (i.e. as close to 12) as possible coordination numbers thus taking into account the fcc-close packed nature of the atomic arrangement in the NPs modeled, as revealed by the simplistic crystal structure-constrained modeling described in the text. Also, atoms were constrained not to come closer than pre-selected distances of closest approach thus taking into account the fact that metallic species may not approach each other much closer than the sum of their radii R_{ij}. Atomic radii used in the RMC simulations corresponded to the well-known metallic radii of Pd, Pt, Ni and Co species [S27].

A relatively new feature [S28, S29] turning the simulations into a hybrid between traditional RMC and MD, was the optimization of model’s energy, i.e. maximizing model’s stability, beyond the level achieved by MD alone. The simultaneous optimization of model’s energy and the difference between model-computed and experimental PDF data is important since if the former or latter are done alone particular structural features of the actual NPs modelled such as, for example, the spread (distribution) of distances between nearby unlike atoms (i.e. NM-TM atomic-pair distances), may end up under or overestimated, respectively. Model’s energy was described by pair-wise (Lennard-Jones type) potentials the parameters of which were taken from literature sources [S30]. Altogether, hybrid RMC simulations aimed at minimizing a residuals function χ^2 involving two major terms, χ_D^2 and χ_P^2, defined as as follows [S12]:

$$\chi_D^2 = \frac{\sum (G_i^{\exp} - G_i^{calc})^2}{\sigma_{G(r)}^2} + \frac{\sum (CN_i^{des} - CN_i^{calc})^2}{\sigma_{CN}^2} + \frac{\sum (R_{ij}^{des} - R_{ij}^{calc})^2}{\sigma_{R_{ij}}^2} \qquad \text{(S4)}$$

$$\chi_p^2 = \frac{\Delta U}{\sigma_{\Delta U}^2} \qquad \text{(S5)}$$

where G_i^{exp} and G_i^{cal} are model-calculated and experimental atomic PDFs for a given value of the real space distance r_i, CN_i^{des} and CN_i^{cal} are preset desired (as close to12 as possible; see above) and model-calculated first atomic coordination numbers, and R_{ij}^{des} and R_{ij}^{cal} are preset desired (as close to the sum of the characteristic for Pt, Pt, Ni and Co atomic radii as possible; see above) and model-calculated first atomic neighbor distances for *ij* atomic pairs, respectively. The term ΔU reflects changes in model’s energy described by Lennard-Jones type potential. Energy changes were triggered by adjusting atomic positions and swapping positions of nearby NM and TM atoms. The σ’s in the denominators of eqs. (S4) and (S5) are weighting factors allowing controlling the relative importance of the individual terms in the residuals function χ^2 being minimized. In the course of simulations the values of σ’s and the rate of swapping the positions of nearby NM and TM atoms were changed several times to increase the chances of finding the global minimum of the residuals function χ^2, instead of a local minimum. The relative importance of fitting well the experimental G(r) data in the region of low-r and higher-r values was also alternated several times (by alternating the region of r values over which G_i^{exp} and G_i^{cal} are compared; see the first term in *eq*. S4). The latter helped refine well the positions and coordination environment of atoms near the surface of the NPs modeled (see Figure S15 for the relationship between the G(r) data at higher r-values and surface structure of metallic NPs). In the final stages of simulations minimizing i) the difference between experimental and calculated atomic PDF data and ii) the energy of model atomic configurations was given preference over maintaining preset CNs and distances of closest atomic approach. The latter though were never violated during the hybrid RMC simulations. The simulations were considered completed when no significant changes in the residuals χ^2 function were observed. The hybrid RMC simulations were done with the help of a new version of the program RMC^{++} [S31]. Note, refining positions of atoms against experimental XRD data is a widely applied technique in crystal structure studies, usually referred to as Rietveld refinement [32]. In essence, hybrid RMC described above may be considered as "real-space" Rietveld refinement with the added benefit of maximizing the stability (minimizing the energy) of the structure model being refined.

x) Determining the degree of alloying in Pd-Ni and Pt-Ni-Co NPs

The degree of chemical ordering in as-synthesized, *ex situ* and *in operando* studied Pd-Ni and Pt-Ni-Co NPs was determined by computing the so-called Cowley's short-range order parameter, α, defined as [S33, S34, S35]:

$$\boldsymbol{\alpha} = \mathbf{1} - \frac{N_{AB}/N_{AT}}{x_B} \qquad \text{(S5)}$$

where x_B is the relative concentration of atoms of type B, N_{AB} is the number of atoms of type B in the first coordination sphere of A-type atoms, and N_{AT} is the total first coordination number of A-type atoms. Note, as defined, α can assume values between +1 and -1. Positive values of α indicate a tendency for phase segregation (clustering) of the particular (i.e. A) atomic species considered. Negative values of α indicate a tendency for alloying of that species (i.e. A) with the other species (i.e. B) in the alloy. To evaluate the tendency of NM (Pd and Pt) atoms in the electrochemically cycled Pd-Ni and Pt-Ni-Co NPs to cluster together eventually forming NM-rich shells at the NP surface, we considered NM and TM (Ni and Co) atoms as A and B-type atoms in *eq. S5,* respectively. To compute Cowley's short-range order parameter we used the partial $N_{NM\text{-}TM}$ and total first coordination number of NM atoms summarized in Figure 11. The coordination numbers are derived from the respective hybrid RMC-refined structure models shown in Figure 10.

Cowley's short-range order parameter for Pd atoms in as-synthesized Pd-Ni NPs and Pd-Ni NPs undergone 3000 electrochemical cycles inside either a standard 3-electrode cell or an operating PEMFC turned out to be 0.04, 0.06 and 0.07, respectively. The values indicated that Pd atoms hardly exhibit any tendency to segregate toward the NP surface.

Cowley's short-range order parameter for Pt atoms in as-synthesized Pt-Ni-Co NPs and Pt-Ni-Co NPs undergone 3000 electrochemical cycles inside either a standard 3-electrode cell or an operating PEMFC turned out to be -0.02, 0.04 and 0.06, respectively. The values indicated that Pt and TM atoms in as-synthesized NPs are well intermixed together. On the other hand, Pt atoms in electrochemically cycled Pt-Ni-Co NPs exhibit a negligible tendency to segregate toward the NP surface, if any.

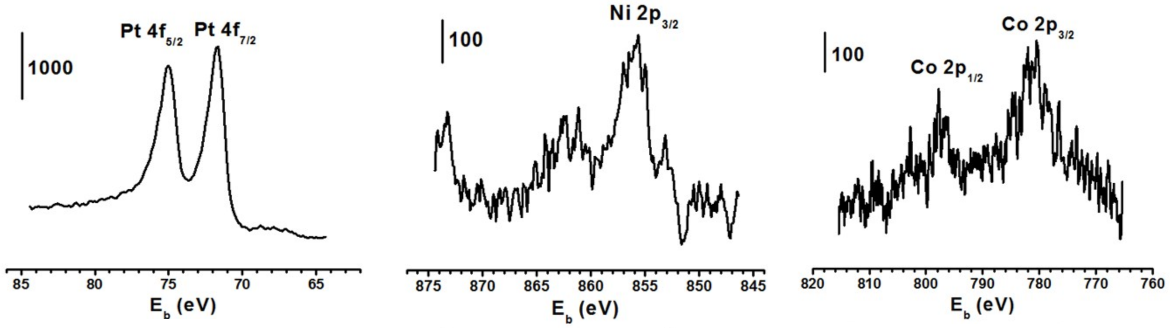

Figure S1. Representative XPS spectra for as-synthesized Pt-Ni-Co ($Pt_{45}Ni_{33}Co_{22}$) NPs in the regions of Pt $4f_{7/2}$ (A), Ni $2p_{3/2}$ (B), and Co $2p_{3/2}$ (C) peaks.

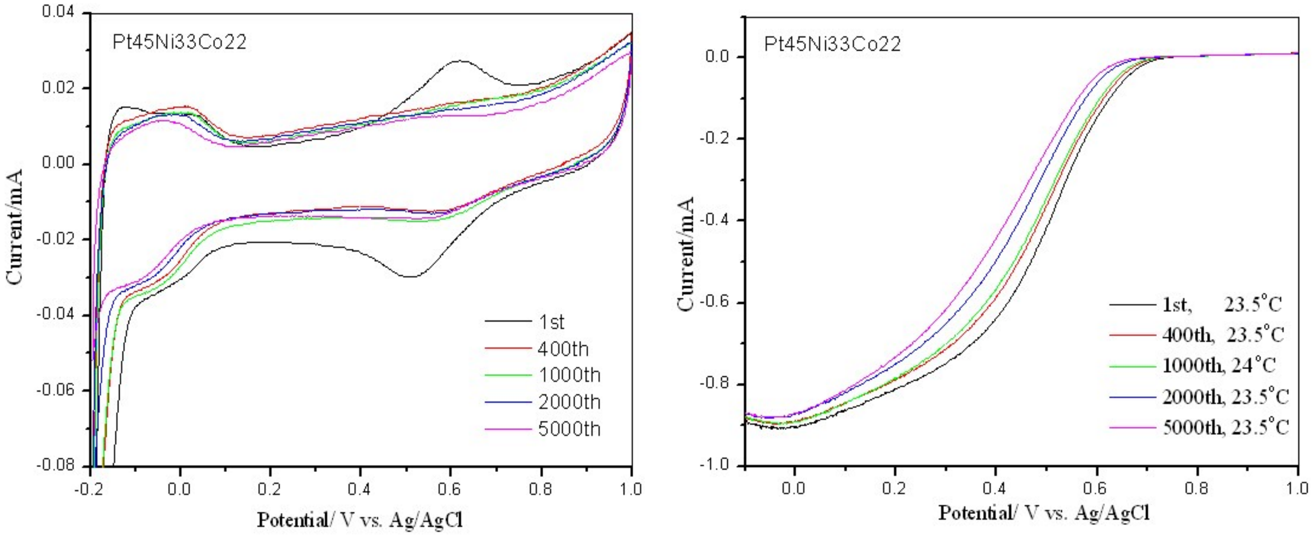

Figure S2. (left) Selected Cyclic Voltammetry (CV) and (right) Rotating Disk Electrode (RDE) data sets for Pt-Ni-Co NPs undergone from one up to 5000 electrochemical cycles between 0.4 V to 1.0 V inside a standard 3-electrode cell. CV data sets are recorded in the range of -0.2 V to +1.0 V with a scan rate of 100 mV/s. RDE data sets are recorded in the range of 0.02 V to 1.2 V with a scan rate of 10 mV/s at 1600 rpm of the working electrode. All potentials were measured with respect to Ag/AgCl (Sat'd KCl) reference electrode. Note both CV and RDE data was taken at room temperature.

Table S1. Evolution of the chemical composition, electrochemical active surface area (ECSA), mass activity (MA) and specific activity (SA) for Pd-Ni and Pt-Ni-Co NPs tested as ORR catalysts at the working electrode of a standard electrochemical cell cycled 400, 1000 and 3000 times between 0.4 V and 1.0 V. Data in the table reflect the ICP-AES, CV and RDE measurements described above. For reference, SA of pure Pt and Pd NPs is about 120 mA/cm^2 and 80 mA/cm^2, respectively [S11].

Cycle #	**Composition per ICP-AES**		**ECSA (m^2/g_{Pd})**	**Mass Activity (mA/mg_{Pd})**	**Specific Activity (mA/cm^2)**
	Pd	**Ni**			
1	30	70	15.3	400	2.60
400	39	61	12.4	127	1.41
1000	46	54	6.5	62	1.18
3000	69	31	2.3	18	0.78

Cycle #	**Composition per ICP-AES**			**ECSA (m^2/g_{Pt})**	**Mass Activity (mA/mg_{Pt})**	**Specific Activity (mA/cm^2)**
	Pt	**Ni**	**Co**			
1	45	33	22	7.1	123	1.74
400	56	25	19	6.9	99	1.42
1000	57	24	19	6.5	90	1.38
3000	59	23	18	6.0	62	1.03

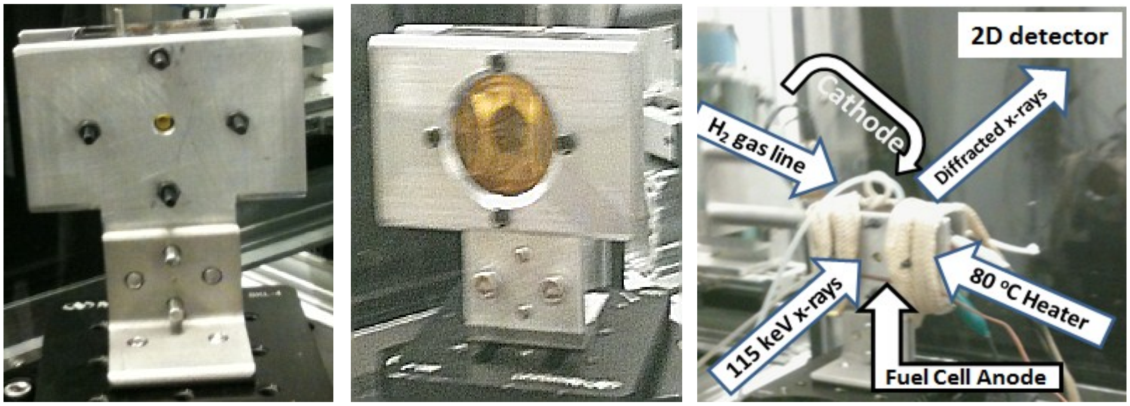

(a) PEMFC anode side (b) PEMFC cathode side (c) the PEMFC in operation

Figure S3. Schematic of a custom-built PEMFC optimized for *in operando* high-energy XRD studies of nanocatalysts for ORR at its cathode. (a) A hole with a diameter of 5 mm is cut through the PEMFC anode end and current collecting plates down to the carbon paper used as a gas (hydrogen) diffusion layer. (b) A spherical window with a diameter of 20 mm is cut through the PEMFC cathode end and current collecting plates down to the carbon papar used as a gas (oxygen) diffusion layer. Both the hole and window are sealed with thin Kapton foils. (c) The PEMFC as set up and used at the beam line 11-ID-C at the Advanced Photon Source, Argonne. In particular, x-rays with energy of 115 keV enter the PEMFC through the hole in its anode side and leave it through the spherical window in its cathode side. The PEMFC cathode side looks into a large area (2D) detector used to collect x-ray intensities diffracted from the PEMFC cathode catalyst. Gas lines and the heater, as wrapped up around the cell, used to maintain pre-desired temperature (~ 80 ^{o}C) during the PEMFC operation are also clearly visible.

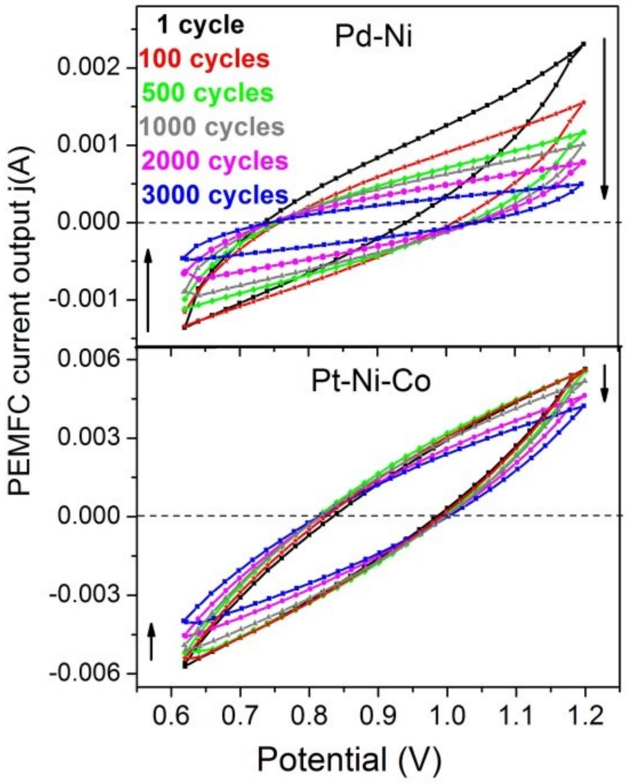

Figure S4. Selected polarization curves (applied voltage vs the resulting current output of the PEMFC) obtained during 3000 potential cycles between 0.6 V and 1.2 V. Curves in the top panel of the Figure are obtained while using Pd-Ni NPs as the PEMFC cathode catalyst. Curves in the bottom panel of the Figure are obtained while using Pd-Ni-Co NPs as the PEMFC cathode catalyst. Arrows emphasize the diminishing current output of the PEMFC with the number of voltage cycles. The current output drops dramatically with the number of PEMFC cycles when Pd-Ni NPs are loaded on the PEMFC cathode. It also drops, though not so dramatically, when Pt-Ni-Co NPs are loaded on the PEMFC cathode instead. The observation, in line with the findings of *ex situ* electrochemical studies (see Table S1 above), indicates that Pd-Ni NPs are inferior to Pt-Ni-Co ones in terms of stability as ORR catalysts. Evidently, the current output of the PEMFC is sensitive to the catalytic activity of NM-TM NPs studied here and so changes in the former can be used as measure of changes in the latter. Note, polarization curves of the type presented here are typical for studies aimed at assessing the stability of NM-TM NPs as catalysts for ORR (e.g. see Figure 2 in refs. [S3]). Also, note, data for the current output shown in the Figure are not normalized per the known amount of ORR catalysts loaded on the PEMFC cathode. The absence of such normalization does not affect in any way the rate of decrease in the current output of the PEMFC with the number of voltage cycles derived from the polarization curves. Data for the current output shown in the Figure, however, are corrected for the resistance current in the PEMFC. That current was measured during a voltage sweep from 0.6 V to 1.2 V with all PEMFC components, including the MEA, in place and ORR shut down.

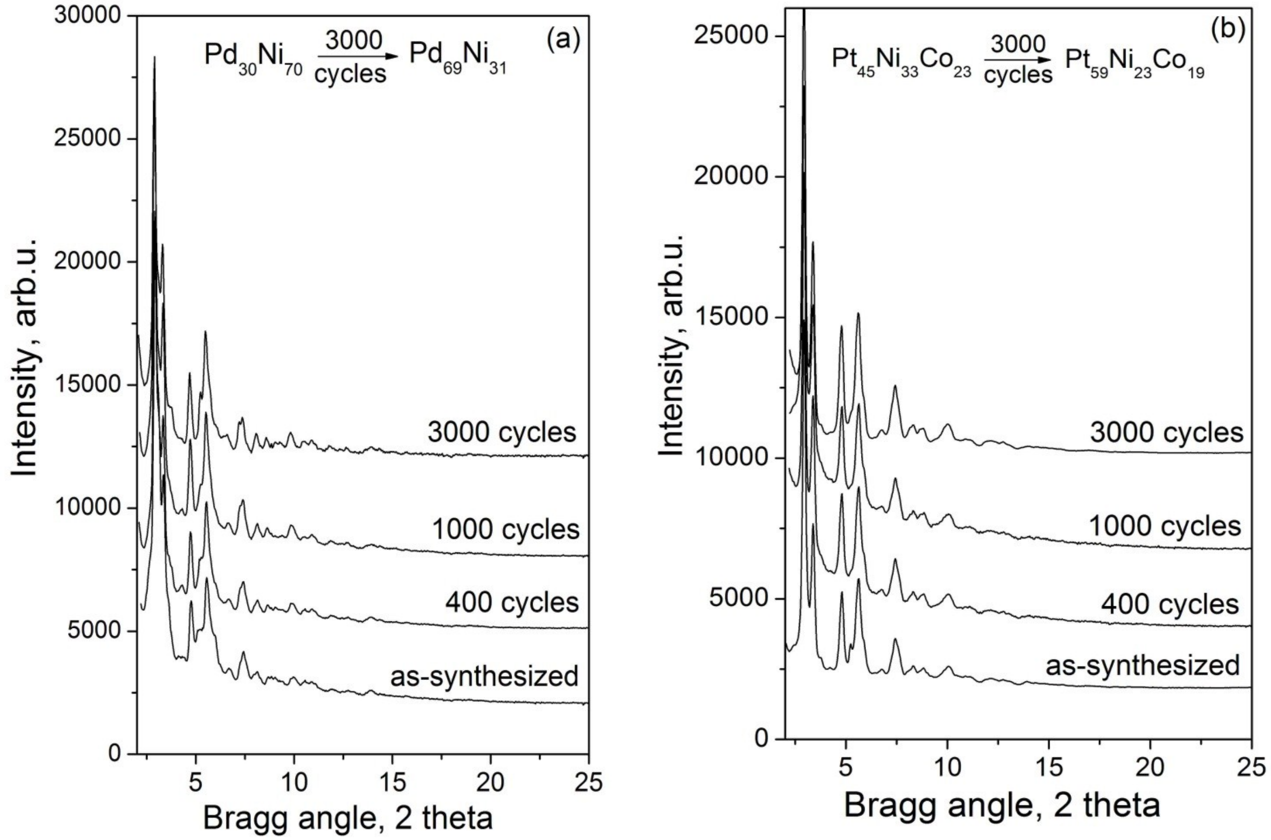

Figure S5. Experimental *ex situ* HE-XRD patterns for (a) Pd-Ni and (b) Pt-Ni-Co NPs as-synthesized and then used as ORR catalysts at the working electrode of a standard electrochemical cell cycled between 0.4 V and 1.0 V. Note, per ICP-AES, the chemical composition of Pd-Ni NP catalysts undergone 3000 cell cycles changes from the initial one of $Pd_{30}Ni_{70}$ to $Pd_{69}Ni_{31}$. That of Pt-Ni-Co NPs undergone 3000 cell cycles changes from the initial one of $Pt_{45}Ni_{33}Co_{22}$ to $Pt_{59}Ni_{23}Co_{18}$. Also, note, the experimental HE-XRD patterns show a few Bragg peak-like features at low diffraction angles and almost no sharp features at higher diffraction angles. The rather diffuse nature of the HE-XRD patterns renders sharp Bragg peak-based procedures for determining the atomic-level structure of bulk metals and alloys inapplicable to the metallic NPs studied here. Lastly, the Bragg-like features in the HE-XRD patterns are seen to get a bit sharper with the number of cell cycles. The observation, in line with the findings of TEM experiments, indicates that both Pd-Ni and Pt-Ni-Co NPs increase in size during the cell cycling.

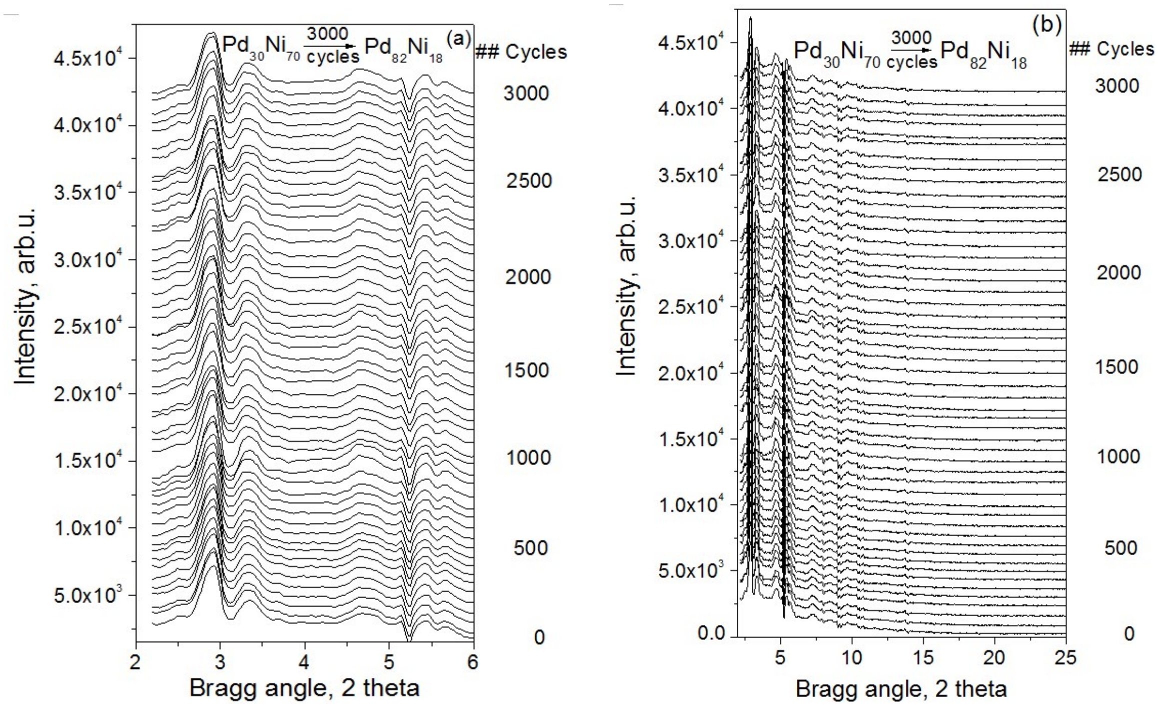

Figure S6. (a) Low-angle part and (b) full-scale experimental HE-XRD patterns for Pd-Ni NPs taken as they are used as an ORR catalyst at the cathode of a PEMFC cycled 3000 times between 0.6 V and 1.2 V. Note, per ICP-AES, the chemical composition of Pd-Ni NPs undergone 3000 PEMFC cycles changes from the initial one of $Pd_{30}Ni_{70}$ to $Pd_{82}Ni_{18}$. Experimental HE-XRD patterns show a few Bragg peak-like features at low diffraction angles and almost no sharp features at higher diffraction angles, a picture typical for metallic NPs < 10 nm. The Bragg-like features in the diffraction patterns are seen to sharpen up with the number of PEMFC cycles. The observation indicates that Pd-Ni NPs continuously increase in size during the PEMFC operation.

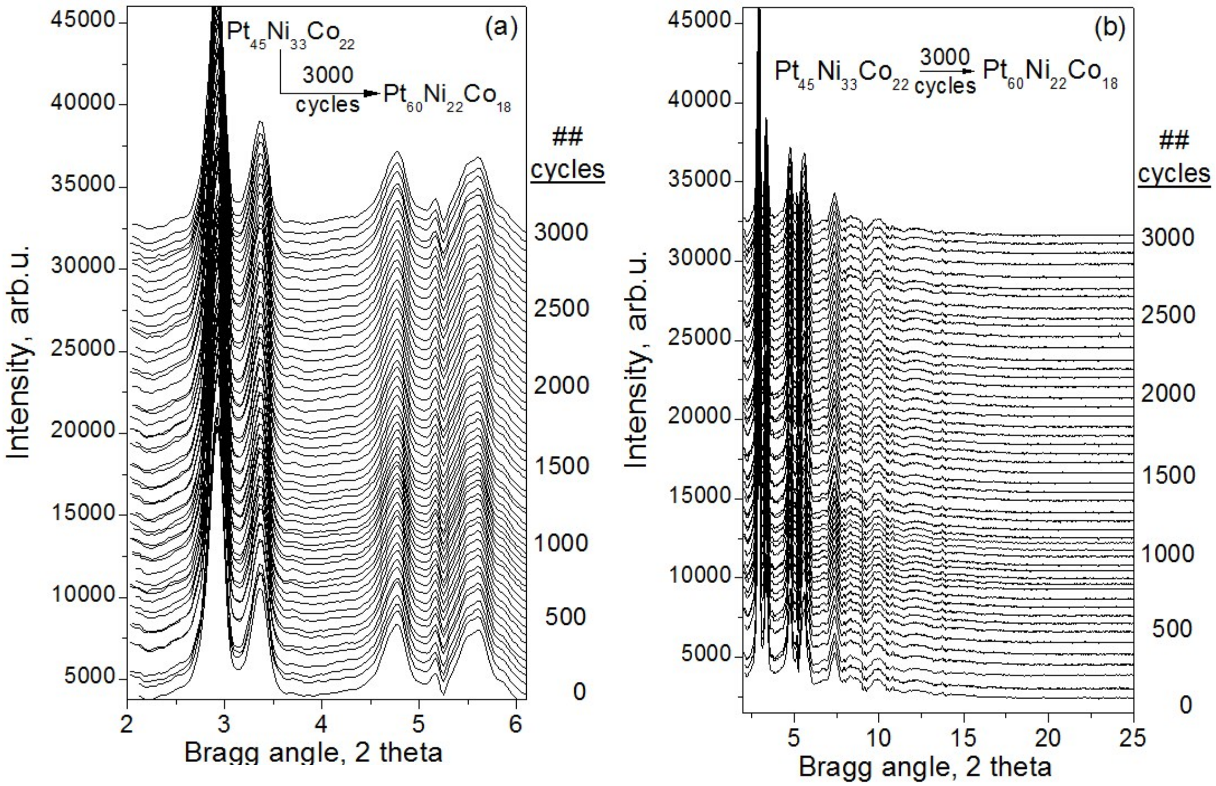

Figure S7. (a) Low-angle part and (b) full-scale experimental HE-XRD patterns for Pt-Ni-Co NPs taken as they are used as an ORR catalyst at the cathode of a PEMFC cycled 3000 times between 0.6 V and 1.2 V. Note, per ICP-AES, the chemical composition of Pt-Ni-Co NPs undergone 3000 PEMFC cycles changes from the initial one of $Pt_{45}Ni_{33}Co_{22}$ to $Pt_{60}Ni_{22}Co_{18}$. Experimental HE-XRD patterns show a few Bragg peak-like features at low diffraction angles and almost no sharp features at higher diffraction angles, a picture typical for metallic NPs < 10 nm. The Bragg-like features in the diffraction patterns are seen to sharpen up with the number of PEMFC cycles. The observation indicates that Pt-Ni-Co NPs continuously increase in size during the PEMFC operation.

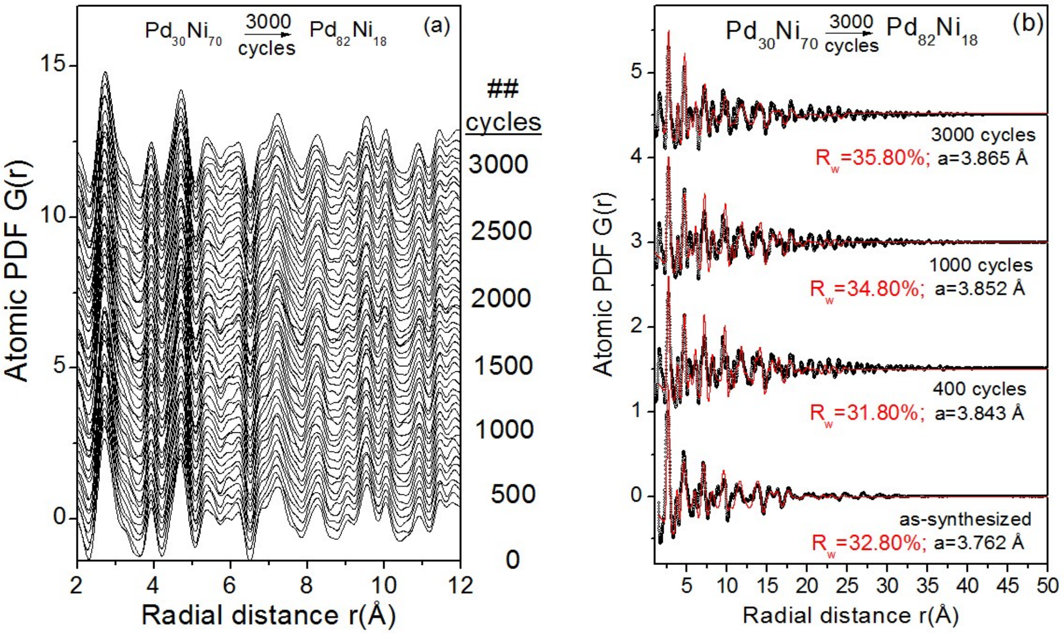

Figure S8. (a) Low-r part of *in operando* atomic PDFs for Pd-Ni NP catalysts derived from the XRD patterns shown in Figure S6. (b) Representative experimental *in operando* atomic PDFs (symbols) from the set shown in (a) and a fcc-type structure model based fits to the PDFs (red lines). The refined "fcc-lattice" parameters are shown by each data set. The respective model quality indicators, R_w, are also shown. Note, per ICP-AES, the chemical composition of Pd-Ni NPs undergone 3000 PEMFC cycles changes from the initial one of $Pd_{30}Ni_{70}$ to $Pd_{82}Ni_{18}$.

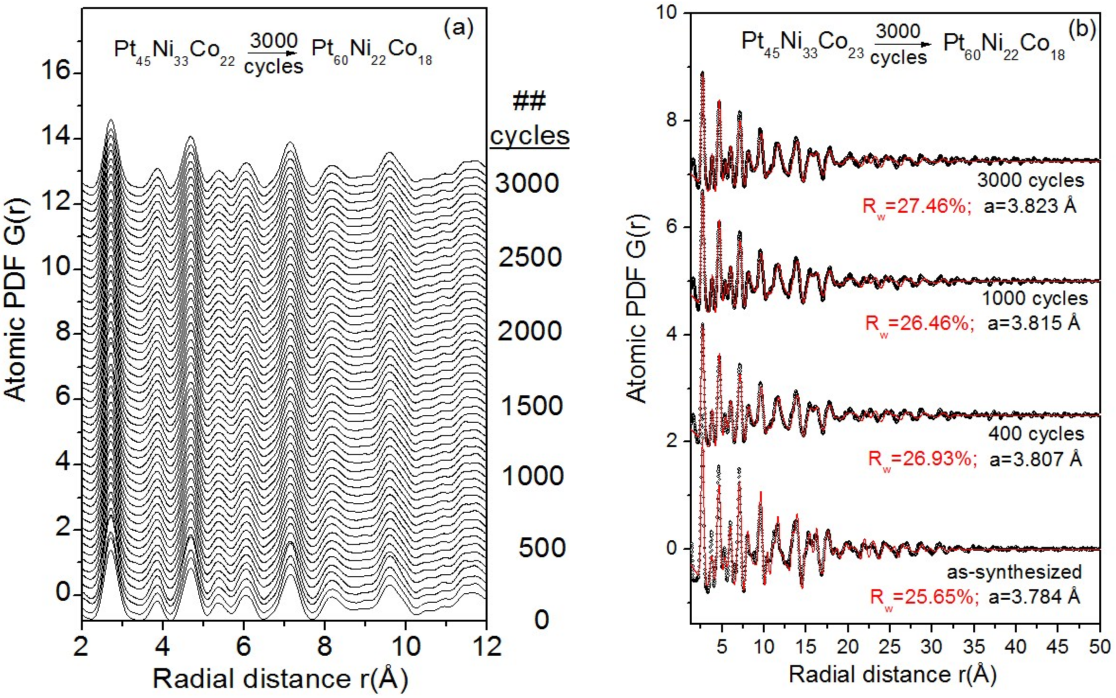

Figure S9. (a) Low-r part of experimental atomic PDFs for Pt-Ni-Co NP catalysts derived from the *in operando* XRD patterns shown in Figure S7. (b) Representative experimental atomic PDFs (symbols) from the set shown in (a) and a fcc-type structure model based fits to the PDFs (red lines). The refined "fcc-lattice" parameters are shown by each data set. The respective model quality indicators, R_w, are also shown. Note, per ICP-AES, the chemical composition of Pd-Ni-Co NPs undergone 3000 PEMFC cycles changes from the initial one of $Pt_{45}Ni_{33}Co_{22}$ to $Pt_{60}Co_{22}Ni_{18}$.

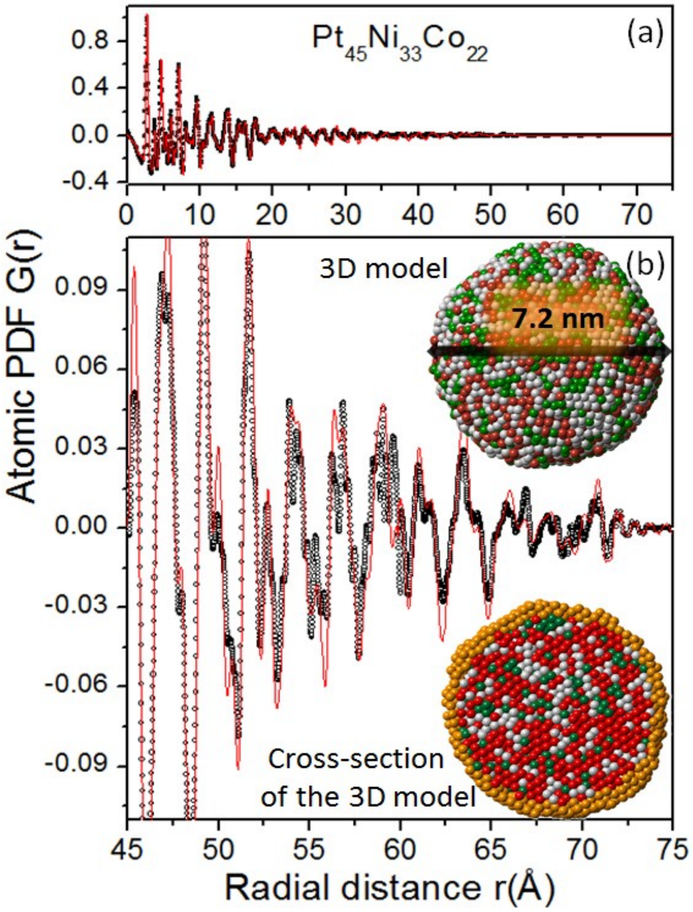

Figure S10. (a) Experimental (symbols) and computed (red line) atomic PDF for 7.3 (±0.6) nm in size Pt$_{45}$Ni$_{33}$Co$_{22}$ NPs studied here. The computed PDF is derived from the respective 3D structure model shown in Figure 10. For convenience, the model is also shown in the top right corner in (b) where the higher-r region of the experimental and model PDF data is emphasized. By definition, the PDF G(r) peaks at distances between pairs of atoms, immediate and all farther neighbors, within the actual NPs studied. The area under the PDF peaks is proportional to the number of pairs of atoms at those distances. Since surface atoms at the opposite sides of NPs are separated the most, experimental G(r)s would show distinct peaks *only* up to distances close to the average size of the respective NPs, as demonstrated in (b). Clearly, G(r) peaks at higher-r distances (55-75 A) would largely reflect pairs of atoms close to the NP surface. Hence, experimental atomic PDFs for metallic NPs used in catalytic applications (usually < 15 nm) are sensitive to the arrangement of atoms at the NP surface. Therefore, 3D models refined against experimental PDF data such as the 3D model shown in (a), including the model's surface, can provide an accurate atomic-level representation of the actual NPs studied. As discussed in the text, this fact may not come as a surprise since atoms at the surface of metallic NPs (< 15 nm) occupy a substantial fraction of their volume and XRD is known to be volume sensitive (down to a few %) technique. For reference, atoms in the top two layers of Pt$_{45}$Ni$_{33}$Co$_{22}$ NPs, highlighted in orange in the slice of the 3D model shown in the lower right corner in (b), are about 25 % of all atoms in these NPs. Pt atoms are in red, Ni and Co atoms are in gray and green, respectively.

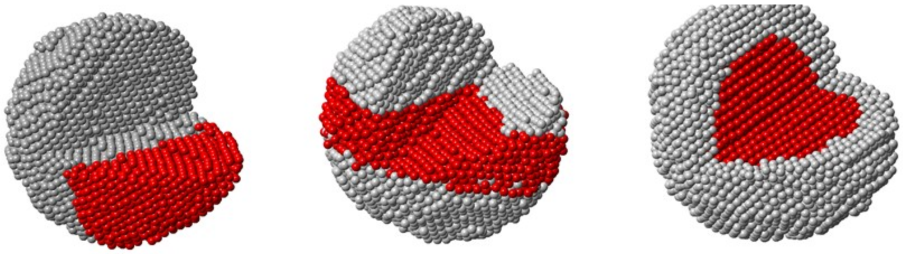

Janus Ni-Pd-Ni sandwich Pd core-Ni shell

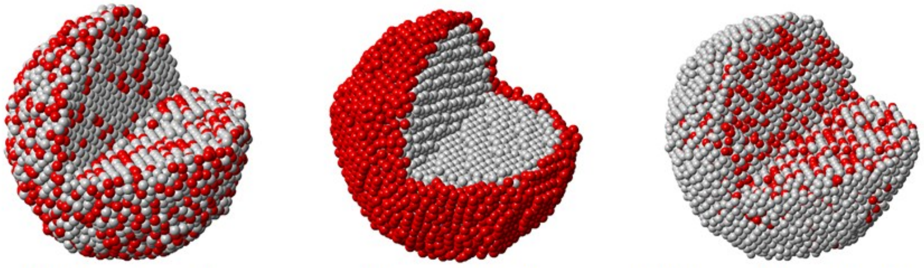

Ni-Pd random alloy Ni core-Pd shell Pd/Ni core-Ni enriched shell

Figure S11. MD built structure models for as-synthesized Pd-Ni ($Pd_{30}Ni_{70}$) NPs featuring various NP phase states, including phase-segregated Janus, Ni-Pd-Ni sandwich, Pd core-Ni shell, Ni core-Pd shell and Pd/Ni core-Ni enriched shell type NPs. A structure model featuring single phase Ni-Pd alloy type NPs is also shown. Comparison between atomic PDFs derived from the models and the respective *ex situ* PDF data is shown in Figure 6. Pd atoms are in red and Ni atoms are in gray.

Janus

Pd-Ni-Pd sandwich

Pd core-Ni shell

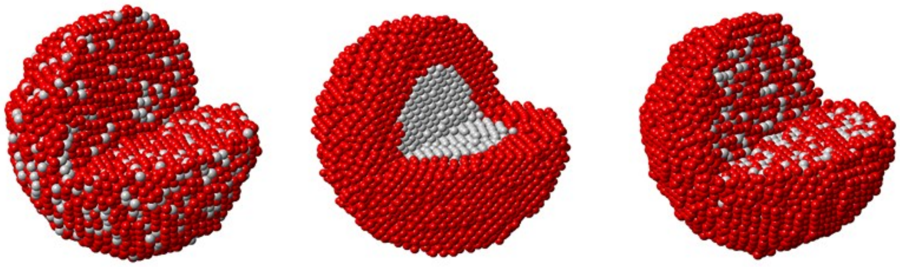

Ni-Pd random alloy

Ni core-Pd shell

Pd/Ni core-Pd enriched shell

Figure S12. MD built structure models for Pd-Ni NPs used as an ORR catalyst at the cathode of a PEMFC cycled 3000 times between 0.6 V and 1.2 V. The chemical composition of NPs is $Pd_{82}Ni_{18}$ as determined by ICP-AES. Models feature NPs of various phase states, including phase-segregated Janus, Pd-Ni-Pd sandwich, Pd core-Ni shell, Ni core-Pd shell and Pd/Ni core-Pd enriched shell type NPs. A structure model featuring single phase Ni-Pd alloy type NPs is also shown. Comparison between atomic PDFs derived from the models and the respective *in operando* PDF data is shown in Figure 15. Pd atoms are in red and Ni atoms are in gray.

SI References:

S1. H. P. Klug and L. E. Alexander in "*X-Ray Diffraction Procedures: For Polycrystalline and Amorphous Materials"*, 2nd Edition, Wiley (1974).

S2. H. A. Gasteiger, S, S, Kosta, B. Sompalii and F. T. Wagner "Activity benchmarks and requirement for Pt, Pt-alloys, and non-Platinum ORR catalysts for PEMFCs" *Appl. Catal. B: Environmental* **56** (2005) 9.

S3. C. A. Rice, Patrick Urchaga, A. O. Pistono, B.W. McFerrin, B. T. McComb and J. Hu "Platinum Dissolution in Fuel Cell Electrodes: Enhanced Degradation from Surface Area Assessment in Automotive Accelerated Stress Tests" *J. Electrochem. Soc.* **16**2 (2015) F1175.

S4. V. Petkov, "RAD, a program for analysis of X-ray diffraction data from amorphous materials for personal computers", *J. Appl. Cryst*., **22** (1989) 387.

S5. T. Egami and S. J. L. Billinge, "Underneath the Bragg peaks: Structural Analysis of Complex Materials.", New York: Pergamon Press, Elsevier Ltd., 2003.

S6. V. Petkov, "Nanostructure by high-energy XRD," *Mater. Today,* **11** (2008) 28.

S7. K. Page, T. C. Hood, T. Proffen and R. B. Neder, "Building and refining complete nanoparticle structures with total scattering data," *J. Appl. Cryst.,* **44** (2011) 327.

S8. W. J. Huang, R. Sun, J. Tao, L. D. Menard, R. G. Nuzzo and J. M. Zuo, "Coordination-dependent surface atomic contraction in nanocrystals revealed by coherent diffraction," *Nature Mater.,* **7** (2008) 308.

S9. D. Marks, “Experimental studies of small particle structures,” *Rep. Prog. Phys.*, **57** (1994) 603.

S10. A. Frenkel, “Solving the 3D structure of nanoparticles,” *Zeitschrift fur Kristallographie,* **222** (2007) 605.

S11. R. Borup, J. Meyers, B. Pivovar, Y. S. Kim, R. Mukundan, N. Garland, D. Myers, M. Wilson, F. Garzon, David Wood, P. Zelenay, K. More, K. Stroh, T. Zawodzinski, J. Boncella, J. E. McGrath, M. Inaba, K. Miyatake, M. Hori, K. Ota, Z. Ogumi, S. Miyata, A. Nishikata, Z. Siroma “Scientific Aspects of Polymer Electrolyte Fuel Cell Durability and Degradation” *Chem. Rev*. 107 (2007) 3904.

S12. V. Petkov, B. Prasai, Y. Ren, S. Shan, J. Luo, P. Joseph and Ch.-J. Zhong “Solving the nanostructure problem: exemplified on metallic alloy nanoparticles” *Nanoscale* **6** (2014) 10048.

S13. S. Shan, V. Petkov, L.Yang, J. Luo, H. Joseph, D. Mayzel, B. Prasai, L. Wang, M. Engelhard and C.J. Zhong " Atomic-structural synergy for catalytic oxidation of CO over Pd-Ni nanoalloys" *J. Am. Chem. Soc.* **136** (2014) 7140.

S14. M. W. Finnis and J. E. Sinclair, "A simple empirical N-body potential for transition metals" *Philos. Mag. A* **50** (1984) 45.

S15. A. P. Sutton and J. Chen, "Long-range Finnis-Sinclair potentials," *Philos. Mag. Lett*., **61** (1990) 139.

S16. Y. Kimura, Y. Qi, T. Cagin and W. Goddard III, "The Quantum Sutton-Chen Many-body Potential for Properties of fcc Metals," *MRS Symp. Ser.,* **554** (1999) 43.

S17. Z. A. Kaszkur and B. Mierzwa, “Segregation in model palladium-cobalt clusters”, *Philos. Mag. A* **77** (1998) 781.

S18. H. Rafii-Tabar and A. S. Sutton, "Long-range Finnis-Sinclair potentials for fcc metallic alloys" *Phil. Mag. Lett.,* **63** (1991) 217.

S19. W. Smith, W. C. Yong and P. M. Rodger, "DL_POLY: Application to molecular simulation.," *Molecular Simulations,* **28** (2002) 86.

S20. B. Prasai, Y. Ren, Sh. Shan,Y. Zhao, H. Cronk, J. Luo, Ch.-J. Zhong and V.Petkov “Synthesis-atomic structure-properties relationships in metallic nanoparticles by total scattering experiments and 3D computer simulations: case of Pt–Ru nanoalloy catalysts” *Nanoscal*e 7 (2015) 8122-8134.

S21. B. H. Toby and T. Egami, "Accuracy of pair distribution function analysis applied to crystalline and non-crystalline materials," *Acta Cryst. A,* **48** (1992) 336.

S22. L. B. Skinner, C. Huang, D. Schlesinger, L. G. M. Petterson, A. Nillson and C. J. Benmore, "Benchmark oxygen-oxygen pair-distribution function of ambient water from x-ray diffraction measurements with a wide Q-range," *J. Chem. Phys,* **138** (2013) 074506.

S23. W. I. F. David, K. Shakland, L. B. McCusker and C. Baerlocher, Structure Determination form Powder diffraction., (Oxford: Oxford University Press., 2002).

S24. B. H. Toby, "R factors in Rietveld analysis: How good is good enough ?," *Powder Diffraction* **21** (2006) 67.

S25. R. McGreevy and L. Pusztai, "Reverse Monte Carlo simulation: a new technique for the determination of disordered structures," *Molec. Simul.,* **1** (1998) 359.

S26. V. Petkov and G. Junchov, "Atomic-scale structure of liquid Sn, Ge and Si by reverse Monte Carlo simulations," *J. Phys.: Condens. Matter* **6** (1994) 10885.

S27. W. B. Pearson in "*The crystal chemistry and physics of metals and alloys"* (New York: Wiley-Interscience, 1972).

S28. T. D. Bennett, A. L. Goodwin, M. T. Dove, D. A. Keen, M. G. Tucker, E. R. Barney, A. K. Soper, E. G. Bithell, J.-C. Tan and A. K. Cheetam, "Structure and Properties of an Amorphous Metal-Organic Framework," *Phys. Rev. Lett.* 1**04** (2010)115503.

S29. N. P. Funnell, M. T. Dove, A. L. Goodwin, S. Parsons and M. G. Tucker, "Local structure correlations in plastic cyclohexane-a reverse Monte Carlo study," *J. Phys.: Cond. Matter,* **25** (2013) 454204.

S30. H. Heinz, R. Vaia, B. Farmer and R. Naik, "Accurate Simulation of Surfaces and Interfaces of Face-Centered Cubic Metals Using 12−6 and 9−6 Lennard-Jones Potentials," *J. Phys. Chem. C,* **112** (2008) 17281.

S31. O. Gereben and V. Petkov, "Reverse Monte Carlo study of spherical sample under non-periodic boundary conditions: the structure of Ru nanoparticles based on x-ray diffraction data," *J. Phys.: Condens. Matter,* **25**, (2013) 454211.

S32. W. I. E. David, ed. In "Struuctuure determination from powder data" (Oxford Unniversity Press: 2003).

S33. J. M. Cowley "An Approximate Theory of Order in Alloys" *Phys. Rev*. **77** (1950) 669.

S34. J. M Cowley "Short- and Long-Range Order Parameters in Disordered Solid Solutions" *Phys. Rev.* **120** (1960) 1648.

S35A. I. Frenkel, Q. Wang, S. I. Sanchez, M. W. Small, RR. G. Nuzzo "Short Range Order in Bimetallic Nanoalloys: An Extended X-ray Absorption Fine Structure Study" *J. Chem. Phys*. **138** (2013) 064202.